Multiple Color Emission of Mechanoluminescence and Photoluminescence from SrZnSO: Bi3+ for Multi-mode Anti-counterfeiting

Yun-Ling Yang
Shanghai University https://orcid.org/0000-0002-7496-3542
Ting Li
Guilin University of Technology
Jia-Yong Yuan
Shanghai University
Yu Zhou
Shanghai University
Qian-Li Li
Shanghai University
Dong-Yun Wan
Shanghai University
Jing-Tai Zhao
Guilin University of Electronic Technology
Zhi-Jun Zhang (zhangzhijun@shu.edu.cn)
Shanghai University

Research Article

Keywords: Mechanoluminescence materials, Multiple Color Emission, Photoluminescence, multi-mode anti-counterfeiting, SrZnSO, Bi3+

Posted Date: August 3rd, 2021

DOI: https://doi.org/10.21203/rs.3.rs-754253/v1

Multiple Color Emission of Mechanoluminescence and Photoluminescence from SrZnSO: Bi^{3+} for multi-mode anti-counterfeiting

Yun-Ling Yang,[a] Ting Li,[c] Jia-Yong Yuan,[a] Yu Zhou,[a] Qian-Li Li,[a] Dong-Yun Wan,[a] Jing-Tai Zhao,[b] Zhi-Jun Zhang [a, *]

[a] *School of Materials Science and Engineering, Shanghai University, Shanghai, 200444, P. R. China.*

[b] *School of Materials Science and Engineering, Guilin University of Electronic Technology, Guilin, 541004, P. R. China.*

[c] *School of Materials Science and Engineering, Guilin University of Technology, Guilin, 541000, P. R. China.*

E-mail addresses: zhangzhijun@shu.edu.cn

Abstract: Mechanoluminescence materials that emit light under mechanical stimulation have attracted widespread attention in sensing, anti-counterfeiting and imaging applications. In this study, a series of novel $Sr_{1-x}Bi_xZnSO$ ($0.001 \leq x \leq 0.1$) samples were synthesized by the method of high temperature solid-state reaction. It is worth noting that the distortion degree of SrO_3S_3 octahedron was increased with increasing Bi^{3+} concentration, and the color manipulated $Sr_{1-x}Bi_xZnSO$ which can emit different photoluminescence (blue to dark blue and finally red) and mechanoluminescence (orange to red) colors are obtained. Moreover, the deep traps can stably store and provide electronic

supplement to shallow traps released under mechanical stimulated. Therefore, devices made of SrZnSO: Bi^{3+} phosphor and polydimethylsiloxane (PDMS) can be used as thermo-mechano-opto three-mode anti-counterfeiting. The ML intensity is linear to the external load, can be utilized for stress sensing or imaging.

1. Introduction

Functional materials that exhibit excellent luminescence properties and chemical stability show a wide range of applications in sensing, detection, memory, display, lighting, optical storage and other fields [1, 2]. Among functional materials, Mechanoluminescence (ML) materials play an important role in intelligent sensors, self-powered lighting or display, and robotics [3]. ML materials can convert the mechanical energy into light emission with the application of various external mechanical stimuli such as compression, impact, stress and friction, even ultrasound [4, 5]. It is worth noting that ML materials show numerous advantages, such as recoverability, wireless detection, intense luminescence, nondestructive analysis, high mechano-optical conversion efficiency, and more importantly, the accurate linear relationship between ML emission intensity and external load in the elastic deformation range providing real-time detection signals of stress in a reliable way [6-8]. It in thus believed that ML materials are potential candidates for applications in many fields, such as stress imaging, damage diagnosis, human health monitoring sensors, electric signature, stress sensors, visualization of stress distribution [6, 9, 10]. For example, the ML intensity of $Sr_{0.97}Al_2O_4$: $Eu_{0.01}$, $Dy_{0.02}$ phosphor composite films is linear with square of impact velocity of the steel ball, which can be used as impact

sensors [11]. Peng *et al.* developed a highly stretchable ML fiber by coating the mixture of ZnS particles and PDMS onto an existing PDMS fiber, and the resulting composite fiber emitted an intensity-tunable light upon stretching and releasing, which can be used for wearable lighting devices [12]. Wang *et al.* developed a flexible pressure sensor based on the ML of ZnS: Mn particles can record the signing habits of people, which can be used for electric signature [13]. To date, many different kinds of ML materials have been developed, such as $SrMgAl_{10}O_{17}$:Eu [14], $ZnAl_2O_4$:Mn [15], $Ca_2Al_2SiO_7$:Eu [16], $SrCaMgSi_2O_7$:Eu [17], $Ca_2Al_2SiO_7$:Ce [18] and so on. However, there are still some problems in the existing ML materials, such as weak ML intensity, limited ML color and structural damage during stress application [19]. Hence, to develop new ML materials with strong ML intensity and tunable emission colors is pressing.

Recently, Liu *et al.* successfully synthesized a novel polar SrZnSO compound crystallized in a polar, non-centrosymmetric hexagonal space group of $P6_3mc$ with lattice parameters a = 3.90442 Å, c = 11.6192 Å and Z = 2 by the method of high temperature solid state reaction [19]. SrZnSO is isostructural to CaZnSO. The substitution of Ca^{2+} by Sr^{2+} in *M*ZnSO (*M* = Ca or Sr) causes a band gap reduction resulting in an influence on the photophysical properties and enhances the optic activity toward the visible region [20]. After the work of Liu *et al.*, Reshak has detailed photophysical properties of SrZnSO and

performed a comprehensive calculation to investigate the influence of substitution of Ca^{2+} (180 pm) by larger Sr^{2+} (200 pm) in *M*ZnSO on the structural properties [21].

Bi can exhibit a variety of valence states, such as Bi^0, Bi^+, Bi^{2+}, Bi^{3+}, and so on [22-24]. Among these valence states, Bi^{3+} is the most stable valence state and have many interesting properties. It is known that Bi^{3+} exhibits a broad and tunable emission band with the electronic configuration of [Xe] $4f^{14}5d^{10}6s^26p^3$ [25]. Moreover, due to the naked 6*s* and 6*p* electrons, Bi^{3+} is sensitive to the surrounding coordination environment [26, 27]. $^1S_0$ is the ground state and $^3P_0$, $^3P_1$, $^3P_2$ and $^1P_1$ are the excited states of Bi^{3+}. The electron transitions from $^1S_0$ to $^3P_0$ and $^3P_2$ are spin forbidden, but the electron transitions from $^1S_0$ to $^3P_1$ and $^1P_1$ are allowed. Due to the strong sensitivity to the coordination environment, the emission of Bi^{3+} can be tuned from ultraviolet to the yellow region due to the different bond lengths, coordination number, lattice symmetry, and so on [28, 29]. Thus, further exploration on the luminescence performance of Bi^{3+} in different hosts is interesting.

In this work, Bi-activated SrZnSO phosphors were synthesized, and their phase purity, site occupation and coordination environment of Bi^{3+} in SrZnSO were investigated by powder X-ray diffraction (XRD) and Rietveld refinement. The morphology and the elemental analysis of $Sr_{1-x}Bi_xZnSO$ were examined to study the particle size and elemental composition. The luminescence properties, optical band gap and trap depth of $Sr_{1-x}Bi_xZnSO$ were investigated in detail to establish the ML mechanism for ML of $Sr_{1-x}Bi_xZnSO$.

2. Experiment

2.1 Methods and synthesis

$Sr_{1-x}Bi_xZnSO$ ($0.001 \leq x \leq 0.1$) samples were synthesized by high temperature solid-state reactions. Original materials ZnS (AR, Sinopharm Chemical Reagent Co., Ltd.), SrO (AR, Zhengzhou Acme Chemical Co., Ltd.), and Bi_2O_3 (99.9%, Shanghai Aladdin Biochemical Technology Co., Ltd.) were weighed, mixed, and ground in an agate mortar. Such stoichiometric mixtures were then sintered under an argon atmosphere in a 1050 ℃ alumina crucible for 10 h in a horizontal tubular furnace. The heating procedure was repeated twice with an intermediate grinding process to reduce phases of impurity. Upon completion of the heating process, samples in the horizontal tubular furnace were cooled down to room temperature and completely ground for characterization.

2.2 Characterization

Powder X-ray diffraction (XRD) designs of arranged tests for stage immaculateness examination were collected on a Rigaku D/max 2500 X-ray diffractometer utilizing Cu Kα (λ = 1.54178 Å) radiation worked at 40 kV and 250 mA in 2θ extend from 10 to 80 ° with a step estimate of 0.02 ° at room temperature. The information for Rietveld examination were collected in a step-scanning mode with a step measure of 0.02 ° and 2 s checking time per step over a 2θ extend from 5 to 130 °, and the Rietveld refinement was performed by utilizing FullProf computer program package [30]. Morphologies, molecule sizes, and energy-dispersive spectroscopy (EDS) natural mapping of sintered tests were inspected employing a filtering electron magnifying instrument (SEM; Zeiss Gemini SEM 300). UV-Vis diffuse reflectance spectra of tests were measured at room temperature on a U-3900H UV/Vis spectrophotometer (HITACHI) and reflection spectra were calibrated with $BaSO_4$. Photoluminescence (PL) and photoluminescence excitation (PLE) spectra were measured

with FLS1000 prepared with a xenon light at room temperature. Radiance rot bends were gotten utilizing an FLS1000 fluorescence spectrometer (Edinburgh Rebellious Ltd., U.K.) and an μF2 streak light was utilized as excitation asset. To assess ML properties of tests, circular composite disks with a distance across of 25 mm and a thickness of 15 mm were arranged by blending $Sr_{1-x}Bi_xZnSO$ powders and optical epoxy tar. These disks were uncovered to bright light (320 nm) for 5 min some time recently location. ML properties were measured with a lab-made framework comprising of a widespread testing machine (AGS-X 10KN STD, Shimadzu), a photomultiplier tube (C13796, Hamamatsu Photonics), and a spectrometer (SR-500i-B1-R, Andor) controlled by a computer. ML pictures of $Sr_{1-x}Bi_xZnSO$ beneath compressive stack were taken with a computerized camera. Thermoluminescence (ThL) spectrum was identified with TOSL-3DS. The test was to begin with uncovered to X-ray for 15 min. It was at that point warmed from room temperature to 500 °C with a warming rate of 1 $°C \cdot s^{-1}$.

3. Results and discussion

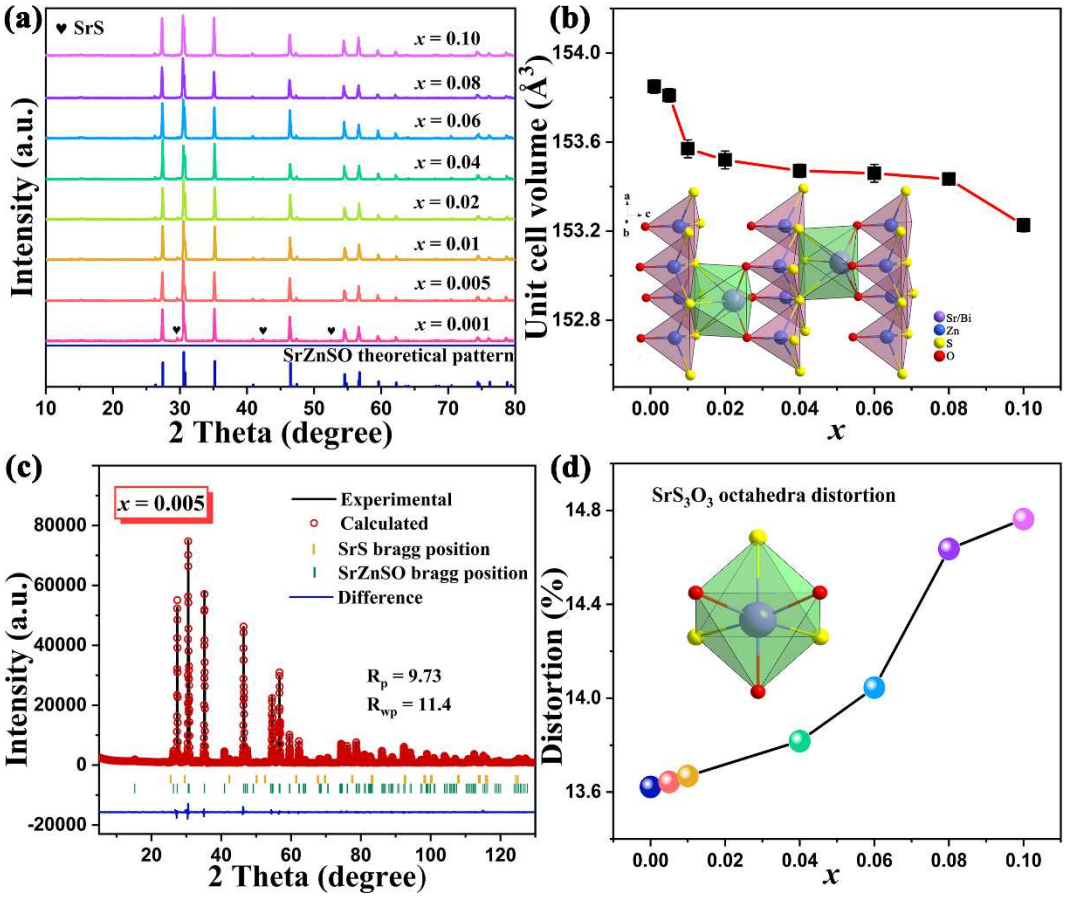

Fig. 1 (a) XRD patterns of $Sr_{1-x}Bi_xZnSO$ ($0.001 \leq x \leq 0.10$). (b) The relationship between Bi^{3+} concentration and the unit cell volume, and the inset graph is crystal structure of $Sr_{0.995}Bi_{0.005}ZnSO$. (c) Rietveld refinement patterns of $Sr_{0.995}Bi_{0.005}ZnSO$. (d) Variation of SrO_3S_3 octahedra distortion with Bi^{3+} concentration ($0 \leq x \leq 0.10$), and the inset graph is structure of SrO_3S_3 octahedra distortion.

The powder XRD patterns of several samples $Sr_{1-x}Bi_xZnSO$ ($0.001 \leq x \leq 0.10$) and SrZnSO theoretical pattern (ICSD No: 431819) are shown in Fig. 1(a). The comparison between $Sr_{1-x}Bi_xZnSO$ patterns and calculated diffraction patterns appears that SrZnSO is the main phase of these samples with a trace of SrS as an impurity phase. The radius of Bi^{3+} (r = 1.03 Å, CN = 6) ion is little smaller than Sr^{2+} (r = 1.18 Å, CN = 6) ion, but the radius of Bi^{3+} ion is much larger than Zn^{2+} (r = 0.74 Å, CN = 6) ion. According to the ionic radius similarity mechanism, when Bi^{3+} ions are introduced into the matrix lattice, Bi^{3+}

ions may occupy the sites of Sr^{2+} ions. As a consequence, substitution of larger Sr^{2+} by smaller Bi^{3+} will lead to lattice shrinkage, as demonstrated in Fig. 1(b). These results indicate Bi^{3+} were successfully incorporated into the samples while maintaining the crystal structures intact. As the representative of $Sr_{1-x}Bi_xZnSO$, we performed the Rietveld refinement for $Sr_{1-x}Bi_xZnSO$ (x = 0, 0.005, 0.04 and 0.08), adopting crystal structure of SrZnSO (ICSD No: 431819) as the initial structure model. As shown in Fig. 1(c) and Fig. S1(a) - (f), the experimental patterns are in good agreement with the theoretical patterns. Primary refinement parameters and point by point crystallographic information are organized in Table 1. The converged refinement results demonstrate that the statistically substituted Bi^{3+} ions on Sr^{2+} sites satisfy the refinements. The shrinkage of cell volume which is agreement with the smaller ionic radius of Bi^{3+} with respect to Sr^{2+} and further indicates that Bi^{3+} ions occupy the sites of Sr^{2+} ions. As shown in the inset graph of Fig. 1(b), the crystal structure of $Sr_{0.995}Bi_{0.005}ZnSO$ is composed of $ZnOS_3$ tetrahedrons and SrO_3S_3 octahedrons. These tetrahedrons and octahedrons are connected to each other to form a three-dimensional layered structure [31]. Rietveld refinement results show that $Sr_{1-x}Bi_xZnSO$ is the hexagonal structure with the space group $P6_3mc$, and the unit cell parameters are: a = 3.91001(2) Å, c = 11.6177(4) Å and V = 153.815(8) Å^3. The refinement results in Table 1, the bond length of Sr-S bonds is inconsistent with Sr-O bonds, indicating that SrO_3S_3 octahedron is distorted. The distortion degree of SrO_3S_3 octahedron can be estimated using the following formula [32]:

$$D = (1/n)\sum_{i=1}^{n}(|L_i - L_{av}|/L_{av}) \quad (1)$$

where D, n, L_i, and L_{av} are distortion degree, number of bonds in SrO_3S_3 octahedron, bond length of Sr|Bi-S or Sr|Bi-O, and average bond length in SrO_3S_3 octahedron, respectively. The distortion degree of SrO_3S_3 octahedron was increased with increasing Bi^{3+} concentration, as shown in Fig. 1(d). In addition, the elemental analysis and morphology of the samples were analyzed by SEM and EDS. The SEM images of the representative samples $Sr_{1-x}Bi_xZnSO$ (x = 0.01, 0.04, 0.08) are shown in Fig. S2. It can be observed that the as-prepared samples are assembled by irregular particles and the particle size distributes about 20-30 μm in diameter.

Table 1 Main refinement parameters and crystallographic data for $Sr_{1-x}Bi_xZnSO$ ($0 \leq x \leq 0.1$).

Compounds	x = 0	x = 0.005	x = 0.01	x = 0.04	x = 0.06	x = 0.08	x = 0.1
a, b /Å	3.9111(2)	3.91001(2)	3.9064(2)	3.9070(9)	3.9053(5)	3.9023(1)	3.9028(7)
c /Å	11.6141(6)	11.6177(4)	11.6207(7)	11.6096(5)	11.6187(4)	11.6117(4)	11.6154(8)
V /Å^3	153.8541(4)	153.815(8)	153.5751(5)	153.4712(8)	153.4606(3)	153.4345(8)	153.2271(3)
$d_{Zn\text{-}S}$ /Å	2.400	2.441	2.440	2.420	2.415	2.421	2.395
$d_{Zn\text{-}O}$ /Å	1.974	1.859	1.859	1.801	1.847	1.964	1.858
$d_{Sr/Bi\text{-}S}$ /Å	3.157	3.157	3.156	3.192	3.187	3.180	3.230
$d_{Sr/Bi\text{-}O}$ /Å	2.400	2.399	2.397	2.417	2.401	2.368	2.399
R_p	13.0	9.73	14.3	14.1	12.8	11.7	11.27
R_{wp}	11.0	12.0	12.2	12.1	14.3	13.0	13.2
χ^2	1.89	8.28	2.65	2.59	4.54	5.62	4.04
SrS (%)	1.57	1.28	2.01	3.02	2.43	0	0

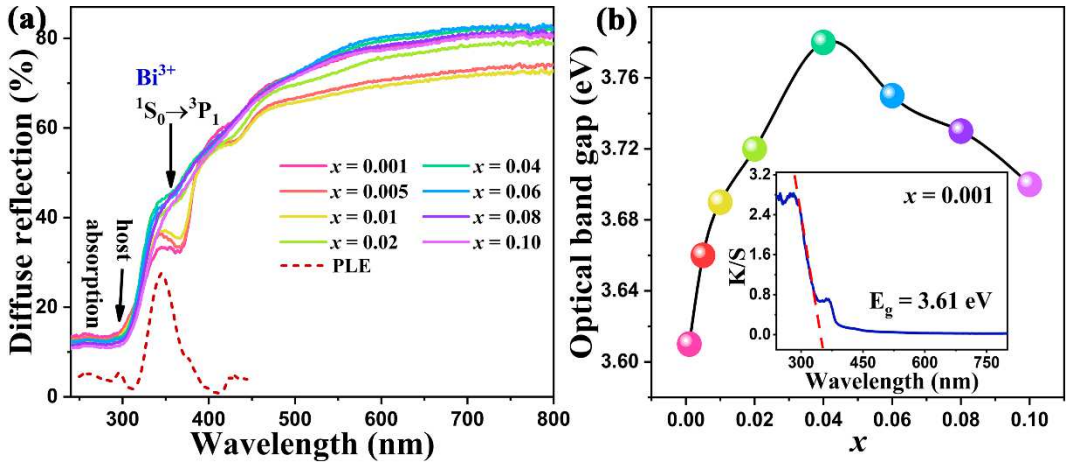

Fig. 2 (a) The diffuse reflectance spectra of $Sr_{1-x}Bi_xZnSO$ ($0.001 \leq x \leq 0.1$) and the PLE spectra of $Sr_{0.99}Bi_{0.01}ZnSO$ (λ_{em} = 613 nm). (b) The correlation between optical band gap (E_g) and different Bi^{3+} concentrations. The inset display the absorption spectrum of $Sr_{0.999}Bi_{0.001}ZnSO$ calculated with the formula of Kubelka-Munk.

The diffuse reflectance spectra of $Sr_{1-x}Bi_xZnSO$ ($0.001 \leq x \leq 0.1$) are shown in Fig. 2(a). $Sr_{1-x}Bi_xZnSO$ ($0.001 \leq x \leq 0.1$) shows high reflection in the range of 600-800 nm. The absorption of $Sr_{1-x}Bi_xZnSO$ ($0.001 \leq x \leq 0.1$) begins to become more intense when the wavelength is below 300 nm. The absorption peaks at about 297 and 345 nm originate from host absorption and $^1S_0 \rightarrow {}^3P_1$ transition of Bi^{3+}. To calculate the optical band gaps of $Sr_{1-x}Bi_xZnSO$, the absorption spectra of $Sr_{1-x}Bi_xZnSO$ were calculated from the diffuse reflectance spectra with the function of Kubelka-Munk [33]:

$$F(R) = K/S = (1-R)^2/2R \quad (2)$$

R is the diffuse reflectance of the sample, K is the absorption coefficient and S is the scattering coefficient. The absorption spectrum of $Sr_{0.999}Bi_{0.001}ZnSO$ calculated with the formula of Kubelka-Munk is shown in the inset of Fig. 2(b). The optical bandgap of $Sr_{0.999}Bi_{0.001}ZnSO$ was calculated to be 3.61 eV on the premise of extrapolation from the

equation of Kubelka-Munk condition to K / S = 0 [34]. It is seen that the values of optical band gap of $Sr_{1-x}Bi_xZnSO$ have increased from 3.61 to 3.78 eV when the concentration of Bi^{3+} is lower than $x = 0.04$, and then decreased to 3.70 eV when the concentration of Bi^{3+} is higher than $x = 0.04$, which is shown in Fig. 2(b). As the electronegativity of Bi^{3+} ion is stronger than that of Sr^{2+}, the covalence of the ligands gradually decreases when Bi^{3+} concentration increased, which leads to the nephelauxetic effect getting weaker. Therefore, the optical band gap of $Sr_{1-x}Bi_xZnSO$ increased when the concentration of Bi^{3+} is lower than $x = 0.04$. However, when the concentration of Bi^{3+} ions is higher, the band gap of $Sr_{1-x}Bi_xZnSO$ decreases due to the appearance of impurity bands and band tails [29].

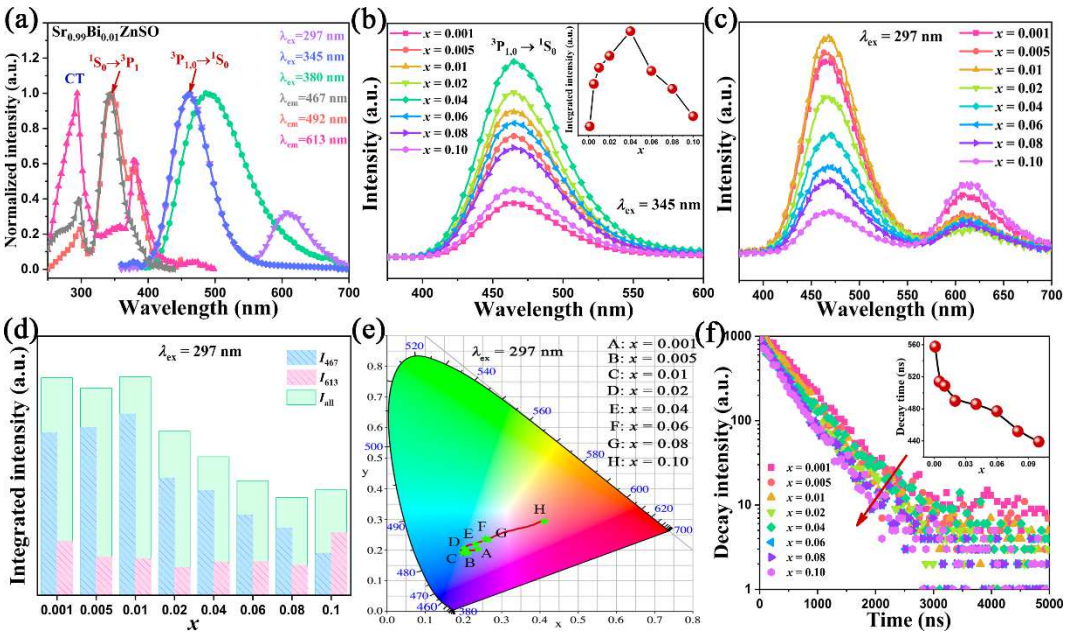

Fig. 3 (a) The normalized PLE and PL spectra and of $Sr_{0.99}Bi_{0.01}ZnSO$ with excitation wavelength at 297, 343 and 380 nm, and monitoring emission wavelength at 462, 492, and 613 nm. (b) and (c) are PL spectra of $Sr_{1-x}Bi_xZnSO$ under excitation wavelength of 345 and 297 nm, and the inset shows the correlation between integrated intensity with excitation wavelength at 345 nm and Bi^{3+} doping concentration. (d) Integrated PL intensity (λ_{ex} = 297 nm) as a function of Bi^{3+} concentration. (e) CIE

chromaticity diagram corresponding to $Sr_{1-x}Bi_xZnSO$ under excitation wavelength of 297 nm. (f) Decay curves of $Sr_{1-x}Bi_xZnSO$ ($0.001 \leqslant x \leqslant 0.1$), and inset shows the decay time as a function of Bi^{3+} doping concentration.

Photoluminescence excitation and emission spectra of $Sr_{0.99}Bi_{0.01}ZnSO$ are shown in Fig. 3(a), the PLE spectrum monitored at 467 nm consists of a strong broad absorption band around 345 nm and a weak absorption band around 297 nm, which are ascribed to the $^1S_0 \rightarrow {}^3P_1$ transition of Bi^{3+} and host lattice absorption, respectively. In addition, the PLE spectrum monitored at 613 nm consists of three absorption bands around 297, 345 and 380 nm. The excitation spectrum of the SrZnSO matrix monitored at 613 nm shown in Fig. S3(a) is in good agreement with this excitation spectrum, indicating that these three absorption peaks are derived from the host lattice absorption. Emission spectra of $Sr_{1-x}Bi_xZnSO$ samples show a wide blue emission band with the center wavelength at 467 nm under the excitation of 345 nm, which is shown in Fig. 3(b). The blue emission band derived from $^3P_{1,0} \rightarrow {}^1S_0$ transitions of Bi^{3+}, and the inset shows the luminescence intensity first increased and then decreased with increasing Bi^{3+} doping concentration. The optimal Bi^{3+} concentration is $x = 0.04$. The luminescence intensity of $Sr_{1-x}Bi_xZnSO$ decreased when Bi^{3+} concentration is higher than $x = 0.04$, which is attributed to the concentration quenching effect. As the concentration of Bi^{3+} ions increase, the distance between the Bi^{3+} ions become smaller, and the non-radiative transition increases, resulting in a decrease in luminescence intensity. The critical distance between the Bi^{3+} ions can be estimated with the following equation [35]:

$$R_c \approx 2[3V/(4\pi X_c N)]^{1/3} \quad (3)$$

R_c, N, X_c, and V are critical distance, the number of sites accessible for the dopant within the unit cell, quenching concentration of activator ion, and unit cell volume, respectively. In $Sr_{1-x}Bi_xZnSO$, values of V, X_c and N are 153.85 $Å^3$, 0.04 and 2, respectively. Consequently, the R_c is estimated to be 15.4 Å, which is quite similar to the results reported in other Bi-activated materials [36, 37]. When concentration quenching effect occurs in $Sr_{1-x}Bi_xZnSO$ phosphors, the electrical multipole interaction between the Bi^{3+} ions play a major role [26, 35]. As shown in Fig. 3(c), emission spectra of $Sr_{1-x}Bi_xZnSO$ samples show a broad blue emission band with the center wavelength of 467 nm and a broad red emission band with the center wavelength of 613 nm under the excitation of 297 nm. Compared with the emission spectrum of SrZnSO host lattice in Fig. S3(b), the broad blue emission band and red emission band are attributed to $^3P_{1,\,0} \rightarrow {}^1S_0$ transition of the Bi^{3+} ions and host emission, respectively. As shown in Fig. 3(d), when the concentration of Bi^{3+} is lower than $x = 0.01$, as the concentration of the Bi^{3+} ions increase, the luminescence intensity of the blue emission band peaking at 467 nm gradually increases, and luminescence intensity of the red emission band peaking at 613 nm gradually decreases. Therefore, when the concentration of Bi^{3+} is lower than $x = 0.01$, the luminescence color of $Sr_{1-x}Bi_xZnSO$ changes from blue to dark blue as the concentration of Bi^{3+} increases. However, when the concentration of Bi^{3+} is higher than $x = 0.01$, as the concentration of Bi^{3+} ions increase, the luminescence intensity of the blue emission band peaking at 467 nm gradually decreases, while the luminescence intensity of the red emission band peaking at 613 nm gradually increases. Therefore, the luminescence color of $Sr_{1-x}Bi_xZnSO$ changes from dark blue to red as the concentration of Bi^{3+} increases as shown in Fig. 3(e).

Decay curves of $Sr_{1-x}Bi_xZnSO$ ($0.001 \leq x \leq 0.1$) phosphors excited at 345 nm and monitored at 467 nm are shown in Fig. 3(f). All the decay curves can be well fitted by the second-order exponential equation [38]:

$$I(t) = A_1 exp(-t/\tau_1) + A_2 exp(-t/\tau_2) + I_0 \quad (4)$$

I (t) and I_0 are luminescence intensity and the initial intensity. A_1 and A_2 are constants. τ_1 and τ_2 are the decay time. The average decay times can be obtained with the following formula:

$$\tau^* = (A_1\tau_1^2 + A_2\tau_2^2)/(A_1\tau_1 + A_2\tau_2) \quad (5)$$

Consequently, the average lifetimes are finally determined to be about 558, 514, 509, 490, 486, 477, 452, 439 ns for x = 0.001, 0.005, 0.01, 0.02, 0.04, 0.06, 0.08 and 0.1, respectively, indicating that the luminescence dynamics of Bi^{3+} are on a nanosecond timescale for $Sr_{1-x}Bi_xZnSO$ samples. As depicted in inset Fig. 3(f), decay time is plotted as a function of Bi^{3+} concentration. The decay time of $Sr_{1-x}Bi_xZnSO$ ($0.001 \leq x \leq 0.1$) decreases with increasing Bi^{3+} concentration. The distance of Bi^{3+} ions gradually decreased and the non-radiative transitions of Bi^{3+} became stronger with increasing Bi^{3+} concentration, resulting in a faster decline in the luminescence lifetime of Bi^{3+}.

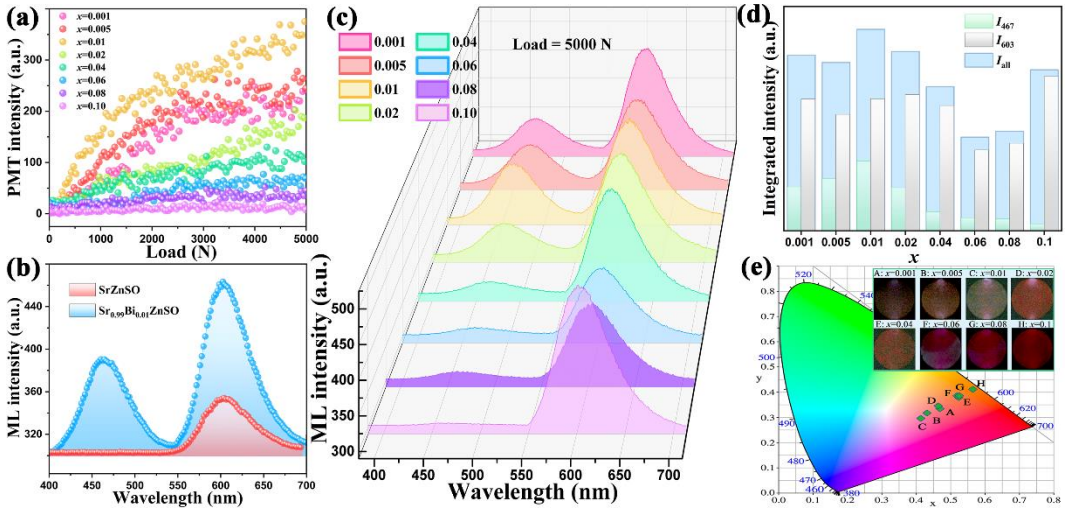

Fig. 4 (a) ML responses of $Sr_{1-x}Bi_xZnSO$ ($0.001 \leq x \leq 0.1$) induced by external load up to 5000 N. (b) Compression induced ML spectra of undoped SrZnSO and $Sr_{0.99}Bi_{0.01}ZnSO$ phosphors combined with resin under the external load of 5000 N. (c) The ML spectra of $Sr_{1-x}Bi_xZnSO$ ($0.001 \leq x \leq 0.1$) phosphors under the external load of 5000 N. (d) Integrated ML intensity of emission peak band at 467and 603 nm as a function of Bi^{3+} concentration under compressive load of 5000 N. (e) CIE chromaticity diagram corresponding to $Sr_{1-x}Bi_xZnSO$ under compressive load of 5000 N, and inset shows the ML images of $Sr_{1-x}Bi_xZnSO$ under compressive load of 5000 N.

ML responses of $Sr_{1-x}Bi_xZnSO$ ($0.001 \leq x \leq 0.1$) induced by compressive load up to 5000 N are shown in Fig. 4(a). With increasing the external load, the ML intensity of $Sr_{1-x}Bi_xZnSO$ ($0.001 \leq x \leq 0.1$) was increased. Maximum ML intensity of $Sr_{1-x}Bi_xZnSO$ was obtained when x = 0.01 and the applied compressive load up to 5000 N. The relation between the $Sr_{1-x}Bi_xZnSO$ phosphors present an approximate linearity of emission intensity against the applied compressive load in a certain range, indicating that $Sr_{1-x}Bi_xZnSO$ phosphors can be used as stress sensors. Compression induced ML spectra of undoped SrZnSO and $Sr_{0.99}Bi_{0.01}ZnSO$ phosphors dispersed into resin under the external load of 5000 N are depicted in Fig. 4(b). ML emission spectra of $Sr_{0.99}Bi_{0.01}ZnSO$ phosphor shows a broad blue emission band with a peak at 467 nm and a broad red emission band with a

peak at 603 nm under compressive load of 5000 N. Furthermore, the ML intensity is sharply increased with the Bi^{3+} ions doped into the SrZnSO host. Compared with the ML emission spectrum of SrZnSO host shows a broad red emission band with a peak at 603 nm, the broad blue ML emission band and red emission band are attributed to $^3P_{1,0} \rightarrow {}^1S_0$ transition of Bi^{3+} ions and the trap of host emission, respectively. Moreover, the ML emission spectra of $Sr_{1-x}Bi_xZnSO$ ($0.001 \leq x \leq 0.1$) phosphors are shown in Fig. 4(c), the two emission bands under the compressive load of 5000 N are around 467 and 603 nm, respectively. As shown in Fig. 4(d), when the concentration of Bi^{3+} ions is lower than x = 0.01, the ML intensity of the blue emission band peaking at 467 nm gradually increases as the concentration of Bi^{3+} ions increase. However, the ML intensity of the blue emission band peaking at 467 nm gradually decreases as the concentration of Bi^{3+} ions increases when $x > 0.01$. As shown in Fig. 4(e), $Sr_{1-x}Bi_xZnSO$ phosphors can emit visible light under compressive load and the ML emission color of $Sr_{1-x}Bi_xZnSO$ gradually changes from pink to red with increasing Bi^{3+} concentration. These results indicate that $Sr_{1-x}Bi_xZnSO$ phosphors have potential for stress imaging.

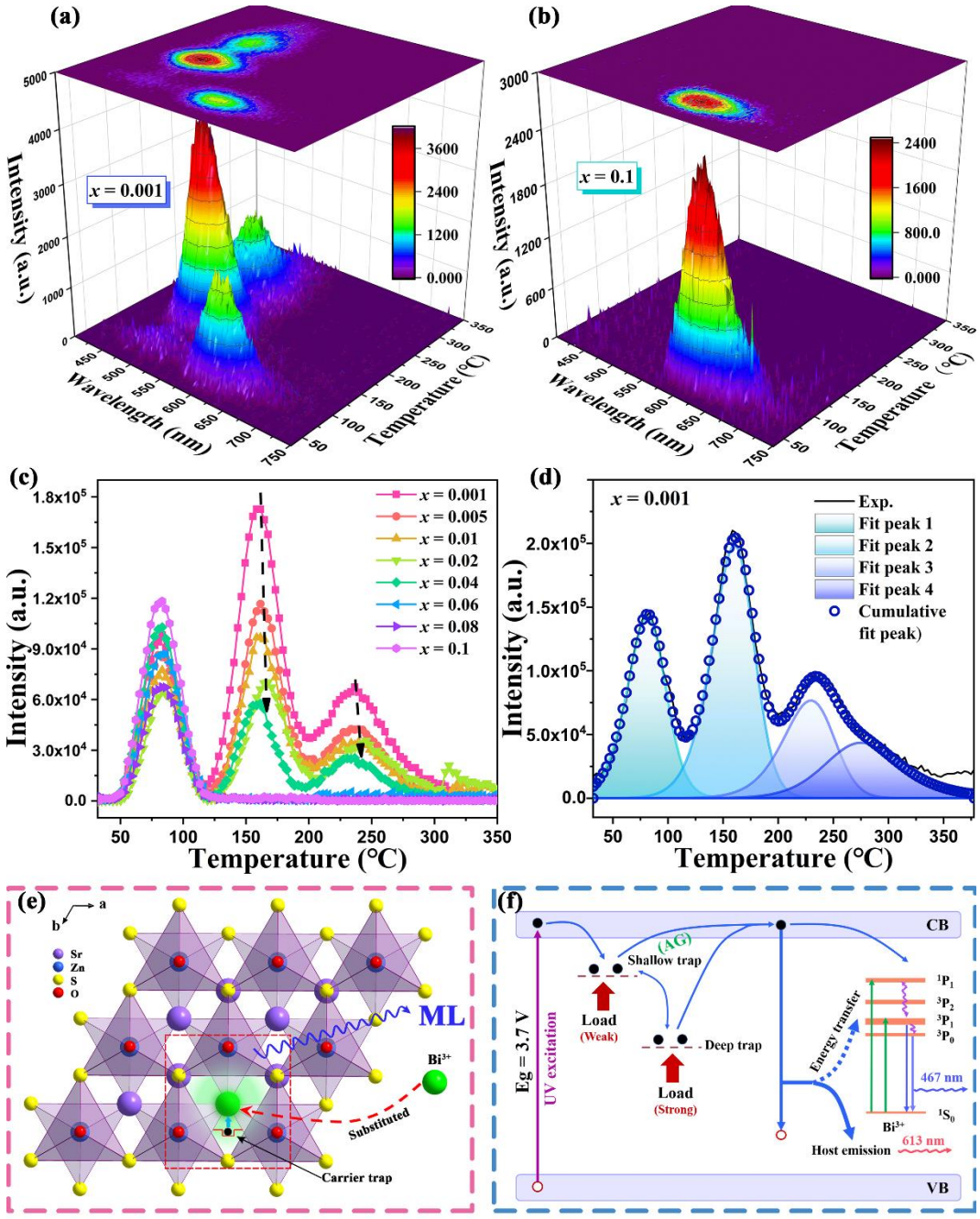

Fig. 5 (a) and (b) 3D thermoluminescence spectra of $Sr_{1-x}Bi_xZnSO$ ($x = 0.001$, 0.01) after excitation with X-ray for 15 min. (c) ThL spectrum of Sr_{1-x} Bi_xZnSO ($0.001 \leq x \leq 0.1$). (d) ThL spectra and fitting curves of $Sr_{0.999}Bi_{0.001}ZnSO$ as a function of temperature. (e) Structural illustration of the proposed stress-assisted trap model based on lattice distortion and emit processes for ML. (f) Schematic diagram of mechanism of $Sr_{1-x}Bi_xZnSO$.

ThL analysis is a common technique for trap characterization in ML materials, including trap depth, density, distribution and traps interactions [35]. The 3D thermoluminescence spectra of $Sr_{1-x}Bi_xZnSO$ (x = 0.0001, 0.01) after excitation with X-ray for 15 min are shown in Figs. (a) and (b). It can be clearly seen that there both appears a peak band with the temperature increasing about 80 °C when the Bi^{3+} ions concentration is 0.001 and 0.1, and it corresponding emission peak at 603 nm. However, the ThL spectra of $Sr_{0.999}Bi_{0.001}ZnSO$ exhibits two peak bands with the temperature at 160 and 236 °C, and it corresponding emission peak at 498 nm. These two peaks are disappeared with the Bi^{3+} ions concentration increasing from 0.001 to 0.06 as shown in Fig. S4. Therefore, all the ThL peak bands are originated from the SrZnSO host traps. Moreover, the 2D ThL spectrum of Sr_{1-x} Bi_xZnSO ($0.001 \leq x \leq 0.1$) are shown in Fig. 5(c), the two peaks shift to high temperature and intensity decreased with x increasing from 0.001 to 0.04. These results reveal that the traps become more deeper and the trap density decrease with the Bi^{3+} ions concentration increasing. However, the strongest ML does not (x = 0.01) appear in the materials with the deepest depth (x = 0.001) or the highest trap concentration (x = 0.04), which implies the complexity of carrier transport in the current ML system [39]. Furthermore, the peak bands at about 80 °C and the trap depth about 0.72 eV are benefited to afterglow [40]. ThL curves of $Sr_{0.999}Bi_{0.001}ZnSO$ as a function of temperature are depicted in Fig. 5(d). The trap depth can be estimated by the multi-peak fitting equation [41]:

$$I(T) = sn_0 exp(-E/kT)\left[1 + (b-1)\, s/v \times \int_{T_0}^{T}(-E/kT')\, dT'\right]^{-b/(b-1)} \quad (6)$$

where $I(T)$ is the ThL intensity, s is the frequency factor, n_0 is the concentration of trapped carriers, E is the trap depth, k is the Boltzmann constant, b is the kinetics order parameter, and v is the heating rate, respectively. Fitted patterns matches well with the experimental patterns. The calculated values of trap depth, frequency factor and kinetic order are summarized in Table S1. The existence of four different ThL peaks indicates that there are four different depth of traps in $Sr_{0.999}Bi_{0.001}ZnSO$ phosphor. The calculated trap depths are 0.72 (peak 1), 0.97 (peak 2), 1.02 (peak 3) and 1.13 (peak 4) eV, respectively. The existence of consecutive multiple trap levels indicates that ML can be excited by mechanical loads with different intensities [5]. In, the schematic diagram of the formation of proposed defects in $Sr_{1-x}Bi_xZnSO$ is shown in Fig. 5(e), the luminescence centers were introduced by doping Bi^{3+} ions that replace Sr^{2+} ions in the host lattice [42]. Due to a non-equivalent substitution, two kinds of defects can be simultaneously created as described by equation:

$$2Bi^{3+} + 3Sr^{2+} \rightarrow 2Bi_{Sr}^{\times} + V_{Sr}^{\cdot\cdot} \quad (7)$$

The Bi^{3+}-related defects $Bi_{Sr}^{\times}$ carrying one positive charge act as the trapping centers of electrons to participate in the trap-related luminescent processes. Furthermore, there are vacancies between Sr^{2+} [43]. To compensate the +3 charge, $V_{Sr}^{\cdot\cdot}$ (where V is denoted as vacancy) with opposite charge should be formed in order to keep the local neutrality [44]. Through non-equivalent substitution and charge-compensated to achieve charge balance, it is expected to expand the design range of ML materials and to study the mechanism. The schematic diagram of mechanism for ML of $Sr_{1-x}Bi_xZnSO$ is shown in Fig. 5(f). Electrons are excited from the valence band (VB) to the conduction band (CB) under ultraviolet

excitation, generating holes in the VB. The electrons excited into the CB are trapped by the traps and migrate from one trap to another with the aid of acquiring (or releasing) thermal energy. Under mechanical stimulation, electrons captured by the shallow traps can be excited to the conduction band by the weak load, while electrons in the deep traps can be excited to shallower contiguous traps, then to the conduction band, or directly to the conduction band by tunneling under the strong load. Part of the electrons that are detraped into the CB excite Bi^{3+} ions and emit blue light with the wavelength of 467 nm by electronic transitions of Bi^{3+} from the $^3P_1$ and $^3P_0$ level to $^1S_0$ level. Another part of the electrons released into the conduction band recombine with the holes in the top of valence band. Part of the energy recombined by electrons and holes is transferred to the Bi^{3+} ions by energy transfer, emitting blue light with a wavelength of 467 nm, and the other part of the combined energy generates red light with the wavelength of 603 nm originated from the trap of host recombine emission.

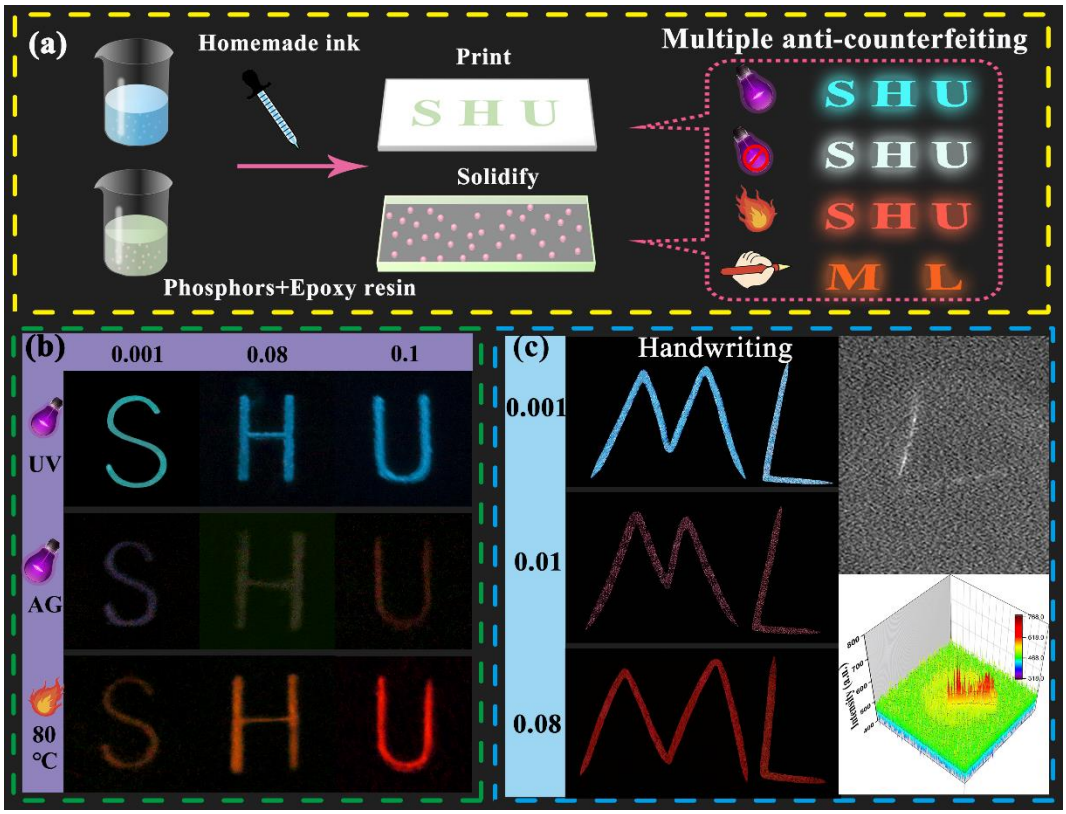

Fig. 6 (a) Schematical diagram of the fabrication process of $Sr_{1-x}Bi_xZnSO$ "inks" and film to record their performance under different stimulated. (b) Picture of drawn "SHU" pattern with handmade ink under ambient light and their performance under the excitation of UV light (365 nm), afterglow (AG) and 80 °C heating in dark environment. (c) Schematical diagram of the signature system with composed $Sr_{1-x}Bi_xZnSO$ (x = 0.001, 0.01 and 0.08) phosphors and PDMS and the recorded pictures in dark environment after handwriting. The inset presents the photo and stress distribution map of handwritten "L".

As aforementioned, the $Sr_{1-x}Bi_xZnSO$ phosphors with different incorporation concentrations of Bi^{3+} exhibit different colors in CIE chromaticity diagram under the excitation of 297 nm wavelength, and the same phenomenon is also recorded when the applied compression load is 5000 N. Inspired by this interesting phenomenon, as shown in Fig. 6(a), the synthesized $Sr_{1-x}Bi_xZnSO$ (x = 0.001, 0.01, 0.08) phosphors will be well dispersed in the handmade "ink" which is the mixture of glycerin and ethylene glycol and

this “ink” is used to draw a “SHU” pattern on the filter paper. Since the ThL peak bands at 80 °C, the dried pattern will be transferred to the dark environment and heated to 80 ℃ for recording its performance. As presented in Fig. 6(b), all the patterns drawn with the “inks” with different Bi^{3+} concentrations emit strong blue-green light under the excitation of 365 nm wavelength. Interestingly, the different colors pattern “SHU” which can emit purple, yellow and red light after turnning off the UV lamp can be obtained with the x = 0.001, 0.08 and 0.1, respectively. Moreover, it can be observed that when heated to 80 ℃ these patterns will emit orange, orange-red, and red light, respectively, which can be attributed to ThL (Fig. 5). This phenomenon is attributed to under heating conditions, the electrons and holes will be released from the traps and finally trapped luminescent center. Moreover, as shown in Fig. 6(c), a film made by dispersing phosphor in PDMS serves as a signature system. The writing photo and the stress distribution map of “L” pattern in handwritten “ML” are collected and shown in the inset. The signature systems with different Bi^{3+} concentrations exhibit different color emissions while handwriting process, which is corresponding to the emission of these samples under loading. Furthermore, with increasing handwriting pressure the writing trace appears to be more precise and brighter. Therefore, thanks to the multi-color emission, the devices made by SrZnSO: Bi^{3+} phosphor and PDMS can be used as multi-mode anti-counterfeiting, which has a great potential in the field of anti-counterfeiting technology.

4. Conclusion

As a summary, novel colorful ML phosphors $Sr_{1-x}Bi_xZnSO$ ($0.001 \leq x \leq 0.1$) were successfully synthesized by high temperature solid-state reactions in this research. ML and PL properties of SrZnSO: Bi^{3+} were investigated for the first time. Rietveld refinement

results indicated that Bi^{3+} ions were occupying the sites of Sr^{2+} ions and the unit cell volume decreased with increasing Bi^{3+} concentration, and the distortion degree of SrO_3S_3 octahedron was increased with the Bi^{3+} ions concentration increasing. The optical band gap of $Sr_{1-x}Bi_xZnSO$ have increased from 3.61 to 3.78 eV, and then decreased to 3.70 eV. The optimal Bi^{3+} concentration for PL is $x = 0.04$. The critical distance between the Bi^{3+} ions was calculated to be 15.43 Å and electrical multipole interaction between the Bi^{3+} ions play a major role in concentration quenching effect. The PL emission color of $Sr_{1-x}Bi_xZnSO$ ($0.001 \leq x \leq 0.1$) changes from blue to dark blue, and then turns red with increasing Bi^{3+} concentration under the 297 nm excitation. The lifetime of $Sr_{1-x}Bi_xZnSO$ ($0.001 \leq x \leq 0.1$) decreased from 558 ns to 439 ns with increasing Bi^{3+} concentration from 0.001 to 0.1. With the increase of Bi^{3+} concentration under compression load, the emission color of ML changes from pink to red. The four different ThL peaks indicate that there are four depth of traps in $Sr_{0.999}Bi_{001}ZnSO$ phosphor. Schematic diagram of mechanism for ML of $Sr_{1-x}Bi_xZnSO$ ($0.001 \leq x \leq 0.1$) is provided. As a new ML material, $Sr_{1-x}Bi_xZnSO$ have great potential in the field of mechanical-optical conversion, stress sensing and stress imaging.

Conflicts of interest

There are no conflicts to declare.

Acknowledgements

This work was supported by the National Natural Science Foundation of China (Grant No. 51772185, U1832159, 11905122), China Postdoctoral Science Foundation (Grant No. 2019M651469).

References

[1] Chen HM, Wu LW, Bo F*, et al.* Coexistence of self- reduction from Mn^{4+} to Mn^{2+}

and elastico- mechanoluminescence in diphase $KZn(PO_3)_3:Mn^{2+}$, *J Mater Chem C* 2019, **7**: 7096-7103.

[2] Tu D, Xu CN, Fujio Y*, et al.* Phosphorescence quenching by mechanical stimulus in CaZnOS:Cu, *Appl Phys Lett* 2014, **105**: 011908.

[3] Zhang HL, Peng DF, Wang W*, et al.* Mechanically Induced Light Emission and Infrared-Laser-Induced Upconversion in the Er-Doped CaZnOS Multifunctional Piezoelectric Semiconductor for Optical Pressure and Temperature Sensing, *J Phys Chem C* 2015, **119**: 28136-28142.

[4] Terasaki N, Yamada H,Xu CN. Ultrasonic wave induced mechanoluminescence and its application for photocatalysis as ubiquitous light source, *Catal Today* 2013, **201**: 203-208.

[5] Wang XS, Zhang JC, Long YZ*, et al.* Novel elastico-mechanoluminescence materials CaZnOS:Mn^{2+} and $CaZr(PO_4)_2:Eu^{2+}$, *J Adv Dielect* 2014, **04**: 1430003.

[6] Su M, Li PH, Zheng SH*, et al.* Largely enhanced elastico-mechanoluminescence of CaZnOS:Mn^{2+} by co-doping with Nd^{3+} ions, *J Lumines.* 2020, **217**: 8.

[7] Fu XY, Zheng SH, Shi JP*, et al.* Investigation of the cyan phosphor $Ba_2Zr_2Si_3O_{12}:Eu^{2+}$, Dy^{3+}: Mechanoluminescence properties and mechanism, *J Alloy Compd* 2018, **766**: 221-228.

[8] Zhang JC, Long YZ, Wang XS*, et al.* Controlling elastico-mechanoluminescence in diphase $(Ba,Ca)TiO_3:Pr^{3+}$ by co-doping different rare earth ions, *RSC Adv* 2014, **4**: 40665-40675.

[9] Li LJ, Wong KL, Li PF*, et al.* Mechanoluminescence properties of Mn^{2+}-doped BaZnOS phosphor, *J Mater Chem C* 2016, **4**: 8166-8170.

[10] Zhang H, Wei Y, Huang X*, et al.* Recent development of elastico-mechanoluminescent phosphors, *J Lumines* 2019, **207**: 137-148.

[11] Jha P, Khare A, Singh PK*, et al.* Ball impact induced elastico-mechanoluminescence for impact sensor, *J. Lumines* 2018, **195**: 40-43.

[12] Zhang J, Bao LK, Lou HQ*, et al.* Flexible and stretchable mechanoluminescent fiber and fabric, *J Mater Chem C* 2017, **5**: 8027-8032.

[13] Wang XD, Zhang HL, Yu RM*, et al.* Dynamic Pressure Mapping of Personalized Handwriting by a Flexible Sensor Matrix Based on the Mechanoluminescence Process, *Adv Mater* 2015, **27**: 2324-2331.

[14] Verma A, Verma A. Synthesis, characterization, mechano-luminescence, thermoluminescence, and antibacterial properties of $SrMgAl_{10}O_{17}$:Eu phosphor, *J Alloy Compd* 2019, **802**: 394-408.

[15] Matsui H, Xu CN,Tateyama H. Stress-stimulated luminescence from $ZnAl_2O_4$:Mn, *Appl Phys Lett* 2001, **78**: 1068-1070.

[16] Tiwari G, Brahme N, Sharma R*, et al.* Fracto- mechanoluminescence and thermoluminescence properties of orange-red emitting Eu^{3+} doped $Ca_2Al_2SiO_7$ phosphors, *J Lumines* 2017, **183**: 89-96.

[17] Zhang HW, Yamada H, Terasaki N*, et al.* Stress-induced mechanoluminescence in $SrCaMgSi_2O_7$:Eu, *Electrochem Solid-State Lett* 2007, **10**: J129-J131.

[18] Akiyama M, Xu CN, Matsui H*, et al.* Recovery phenomenon of mechanoluminescence from $Ca_2Al_2SiO_7$:Ce by irradiation with ultraviolet light, *Appl Phys Lett* 1999, **75**: 2548-2550.

[19] Liu W, Lai KT, Eckhardt K*, et al.* Synthesis and characterization of sulfide oxide

SrZnSO with strongly polar crystal structure, *J Solid State Chem* 2017, **246**: 225-229.

[20] Reshak AH, Abbass NM, Bila J*, et al.* Noncentrosymmetric Sulfide Oxide MZnSO (M = Ca or Sr) with Strongly Polar Structure as Novel Nonlinear Crystals, *J Phys Chem C* 2019, **123**: 27172-27180.

[21] Reshak AH. Sulfide oxide XZnSO (X = Ca or Sr) as novel active photocatalytic water splitting solar-to-hydrogen energy conversion, *Appl Catal B-Environ* 2018, **225**: 273-283.

[22] Yang YL, Zhou Y, Pan DJ*, et al.* The luminescence properties of CaZnOS:Bi^{3+}, Sm^{3+}, Li^{+} phosphors with tunable emissions and energy transfer for white emission, *J Lumines* 2019, **206**: 578-584.

[23] Pan DJ, Yang YL, Yang XC*, et al.* The effect of site occupation and valence state of Bi on the luminescence properties of Bi-activated oxysulfide MZnOS (M = Ca, Ba) with layer structure, *J Alloy Compd* 2018, **742**: 1037-1045.

[24] Yang WY, Chen Y, Gao S*, et al.* Post-illumination activity of Bi_2WO_6 in the dark from the photocatalytic "memory" effect, *J Adv Ceram* 2021, **10**: 355-367.

[25] Xie W, Tian CX, Lyu FC*, et al.* Toward temperature-dependent Bi^{3+}-related tunable emission in the YVO_4:Bi^{3+} phosphor, *J Am Ceram Soc* 2019, **102**: 3488-3497.

[26] Yang P, Guo ZY, Sun ZS*, et al.* An insight of luminescence properties of Bi^{3+}-activated $K_2BaCa(PO_4)_2$ phosphors, *Solid State Sci* 2019, **92**: 1-5.

[27] Wang L, Gui MQ, Jin HB*, et al.* Temperature dependent conductivity of $Bi_4Ti_3O_{12}$ ceramics induced by Sr dopants, *J Adv Ceram* 2018, **7**: 256-265.

[28] Wu QS, Chen X, Chen HD*, et al.* A novel pale-yellow $Ba_2ZnGe_2O_7$:Bi^{3+} phosphor

with site-selected excitation and small thermal quenching, *J Am Ceram Soc* 2019, **102**: 6068-6076.

[29] Li X, Li PL, Wang ZJ*, et al.* Color-Tunable Luminescence Properties of Bi^{3+} in $Ca_5(BO_3)_3F$ via Changing Site Occupation and Energy Transfer, *Chem Mater* 2017, **29**: 8792-8803.

[30] Roisnel T,Rodriguez-Carvajal J. WinPLOTR: A Windows tool for powder diffraction pattern analysis, *Mater Sci Forum* 2001, **378**: 118-123.

[31] Ting Li, Yun-Ling Yang, Yu-Ting Fan*, et al.* Pr^{3+} Doped SrZnOS to Achieve Tunable Mechanoluminescence Color and Mechanoluminescence Mechanism, *Chinese J Lumin* 2021, **42**: 11.

[32] Du QP, Feng SW, Qin HM*, et al.* Massive red-shifting of Ce^{3+} emission by Mg^{2+} and Si^{4+} doping of YAG:Ce transparent ceramic phosphors, *J Mater Chem C* 2018, **6**: 12200-12205.

[33] Zhang ZJ, Ten Kate OM, Delsing A*, et al.* Photoluminescence properties of Pr^{3+}, Sm^{3+} and Tb^{3+} doped $SrAlSi_4N_7$ and energy level locations of rare-earth ions in $SrAlSi_4N_7$, *J Mater Chem C* 2014, **2**: 7952-7959.

[34] Liao M, Mu ZF, Zhang SA*, et al.* A red phosphor $Mg_3Y_2Ge_3O_{12}:Bi^{3+}$, Eu^{3+} with high brightness and excellent thermal stability of luminescence for white light-emitting diodes, *J Lumines* 2019, **210**: 202-209.

[35] Zheng WX, Wu HY, Ju GF*, et al.* Crystal field modulation-control, bandgap engineering and shallow/deep traps tailoring-guided design of a color-tunable long-persistent phosphor (Ca, Sr)$Ga_4O_7:Mn^{2+}$, Bi^{3+}, *Dalton Trans.* 2019, **48**: 253-265.

[36] Yang YL, Li QL, Yang XC*, et al.* Color manipulation of Bi^{3+}-activated CaZnOS

under stress with ultra-high efficiency and low threshold for anticounterfeiting applications, *J Mater Chem C* 2020, **8**: 3308-3315.

[37] Hua H, Feng SW, Ouyang ZY*, et al.* YAGG: Ce transparent ceramics with high luminous efficiency for solid-state lighting application, *J Adv Ceram* 2019, **8**: 389-398.

[38] Li K, Fan J, Shang MM*, et al.* $Sr_2Y_8(SiO_4)_6O_2:Bi^{3+}/Eu^{3+}$: a single-component white-emitting phosphor via energy transfer for UV w-LEDs, *J Mater Chem C* 2015, **3**: 9989-9998.

[39] Zhang JC, Gao N, Li L*, et al.* Discovering and Dissecting Mechanically Excited Luminescence of Mn^{2+} Activators via Matrix Microstructure Evolution, *Adv Funct Mater* 2021, **31**: 2100221.

[40] Yang YL, Yang XC, Yuan JY*, et al.* Time-Resolved Bright Red to Cyan Color Tunable Mechanoluminescence from CaZnOS: Bi^{3+}, Mn^{2+} for Anti-Counterfeiting Device and Stress Sensor, *Adv Opt Mater* 2021, DOI: 10.1002/adom.202100668: 12.

[41] Zhou H, Du YD, Wu C*, et al.* Understanding the mechanoluminescent mechanisms of manganese doped zinc sulfide based on load effects, *J Lumines* 2018, **203**: 683-688.

[42] Yang YL, Yuan JY, Fan YT*, et al.* Efficient energy transfer from Bi^{3+} to Mn^{2+} in CaZnOS for WLED application, *Dalton Trans* 2021, DOI: 10.1039/D1DT01623G.

[43] Sun RX, Liu TY, Wu KL*, et al.* First-principles study of electronic structure and magnetism in SrO crystal contained cation defects, *J Magn Magn Mater* 2021, **522**: 5.

[44] Han J, Li LJ, Peng MY*, et al.* Toward Bi^{3+} Red Luminescence with No Visible Reabsorption through Manageable Energy Interaction and Crystal Defect Modulation in Single Bi^{3+}-Doped $ZnWO_4$ Crystal, *Chem Mater* 2017, **29**: 8412-8424.

Supplementary Files

This is a list of supplementary files associated with this preprint. Click to download.

- Supplementalmaterial.docx